Contributions to the defocusing effect on pole figure measurements by X-ray diffraction

J. Palacios Gómez, R.S. Salat Figols, A. Jiménez Jiménez, and T. Kryshtab
Escuela Superior de Física y Matemáticas, Instituto Politécnico Nacional,
Av. Instituto Politécnico Nacional S/N, 07738 México D.F., México,
e-mail: palacios@esfm.ipn.mx

Received 20 October 2014; accepted 18 May 2015

A simple method, considering a parallel beam approximation has been made to reproduce the main features of the defocusing effect, observed when pole figures are measured with the Schulz reflection technique using X-ray diffraction. A Lorentzian curve was used to approximate the primary beam profile. This method applied to low index reflections of copper and silver shows qualitatively and partially quantitatively, the extent the elongation of the ellipse resulting from the intersection of the beam with the tilted sample causes the defocusing effect. Differences observed experimentally are attributed mainly to the divergence of the beam, but also partially to the particular primary beam profile. Additionally, measurements with two different vertical heights of the receiving slit, *i.e.* the measured arch length of the Debye-Scherrer ring, indicate that this parameter plays no role in defocusing.

Keywords: X-ray diffraction; texture.

PACS: 82.80.Ej

1. Introduction

The defocusing effect, observed when measuring pole figures of textured polycrystals by X-ray diffraction using the conventional Schulz reflection method, consists of a diminution of the diffracted beam for middle to large tilt angles of the sample, arising from the elongation of the irradiated area of the tilted sample, and enhanced by the divergence of the beam, assuming no misalignment of the Eulerian cradle. The aim of this work is to test to what extent, a simple model of a parallel beam can reproduce the main features of defocusing, and to what extent the beam divergence increases this effect. Therefore, it is not expected that the defocusing curves resulting from this treatment reproduce accurately the curves obtained experimentally. Also since different reflections (with different Bragg angles) produce different sizes of the Debye-Scherrer rings, it could be expected that differences of the arch segment of the Debye-Scherrer ring captured by the detector could play some role in defocusing. This is also tested here.

Since the introduction of the Schulz technique [1], several detailed and sophisticated theoretical treatments to correct for the defocusing effect have been published [2,3,4,5], but up to now, practical corrections for this phenomenon are rather made through the measurement of defocusing curves from powders of the same material as the samples. Other techniques have also been devised [6] involving the preparation of samples, and more recently defocusing has been avoided using parallel beam approaches, as for example through the application of polycapillary collimators, the so called "X-ray lenses" [7]. Parallel beam techniques produce no defocusing because no other reflection is expected near the reflection under investigation, and thus, there is no need of a slit in front of the detector, as in the conventional Schulz technique. But also other new techniques based on profile analysis, as the Combined Analysis (CA) [8] and Generalized Pole Figures (GPF) [9,10] do not need the conventional defocusing correction. However, these techniques require more sophisticated measurements and evaluations. To have a simple method to estimate the main features of defocusing for conventional laboratories, although not accurate enough as a correction technique, is useful, and this is the aim of this work.

2. Foundations of the method

Figure 1 shows a typical experimental layout of the sample, to measure a pole figure by the Schulz method. Collimation is made through a pinhole of radius R, and a broad vertical slit, designed to let the whole integrated diffracted intensity at low tilt angles, stays in front of the detector.

The incident as well as the diffracted beams will be considered non divergent. A right cylinder of radius R is assumed as the primary beam, with a cylindrical intensity profile $g(r)$. The irradiated zone is then found as the intersection of the beam with the inclined plane of the sample surface, and this zone, which is an inclined elongated ellipse, is projected towards the slit. The portion of the projected ellipse within the slit, weighted by the intensity profile is calculated as the intensity registered by the detector. Primary beam profile was determined by a detector scan. For simplicity, total reflection is assumed at the sample surface.

The cylinder of the primary beam, assumed first along the Z axis, namely: $x^2 + y^2 = R^2$, is rotated $\pi/2 - \theta$ counterclockwise around the X axis, to make it coincide with the incident beam. The equation of the cylinder is then

$$x^2 + y^2 \sin^2\theta + z^2 \cos^2\theta + 2yz \sin\theta \cos\theta = R^2 \qquad (1)$$

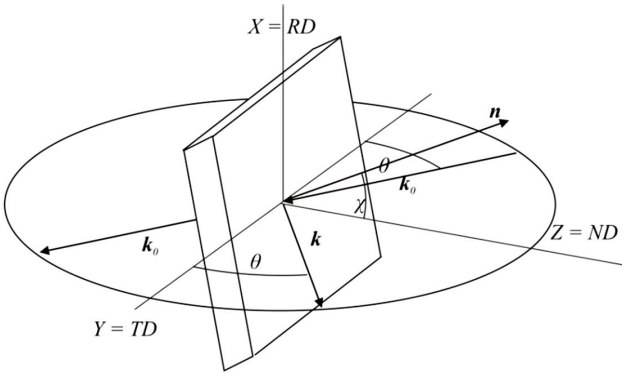

FIGURE 1. Experimental layout to measure a pole figure. Cartesian axes are associated to sample characteristics as usual, namely: X along the rolling direction, Y along the transversal direction, and Z along the normal direction; $\boldsymbol{n}$ is the normal to the powder sample tilted an angle χ around the Y axis; θ is the Bragg angle, and $\boldsymbol{k}_0$ and $\boldsymbol{k}$ are the incident and diffracted beams respectively.

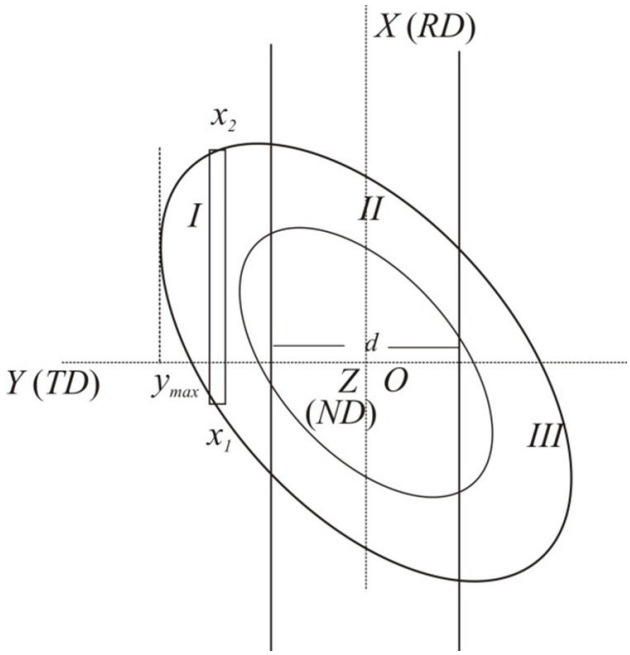

FIGURE 2. Ellipse of the diffracted beam cross section. d is the width of the slit in front of the detector. The inner ellipse shows only a curve of equal intensity. This figure shows the general case where the diffracted beam cross section has already exceeded (zones I and III) the area of the slit (II).

The plane of the sample surface tilted at a general angle χ, is described by the equation $\mathbf{r} \cdot \hat{\mathbf{n}} = 0$, where $\hat{\mathbf{n}} = (\sin\chi, 0, \cos\chi)$ is a unitary vector normal to the sample surface, and therefore at an angle χ with respect to the Z axis on the XZ plane, *i.e.*

$$x\sin\chi + z\cos\chi = 0$$

or

$$z = -xtg\chi. \tag{2}$$

The limit of the irradiated zone on the sample surface is a curve obtained by the intersection of the cylinder given by (1) with the surface given by (2). In order to determine how this curve looks like to an observer at the detector place, the Cartesian coordinate system is rotated $\pi/2 - \theta$ clockwise around the X axis. The cylinder (1) and the plane (2) in the new Cartesian system are respectively

$$x^2 + (y\cos 2\theta - z\sin 2\theta)^2 = R^2. \tag{3a}$$

and

$$z\sin\theta = -xtg\chi + \cos\theta. \tag{3b}$$

Substituting (3a) in (3b), one obtains

$$x^2(1 + 4\cos^2\theta tg^2\chi) + y^2 - 4xy\cos\theta tg\chi = R^2 \tag{4}$$

which is interpreted as the projection of the curve on the new XY plane. This is the cross section of the diffracted beam, as seen by the observer at the place of the detector. All curves of equal diffracted intensity have also this profile, with the variable r instead of R, as shown in Fig. (2). However, only radiation passing through the slit, is registered by the detector.

From (5) it is easy to show that the left maximum value of y is given by

$$y_{\max} = R\sqrt{1 + (2\cos\theta tg\chi)^2} \tag{5}$$

For small χ angles, the whole beam passes through the slit, as long as

$$|y_{\max}| \leq \frac{d}{2}$$

And the critical angle χ_0 at which the ellipse starts to exceed the slit dimension is when

$$y_{\max} = \frac{d}{2}$$

i.e.

$$\chi_0 = tg^{-1}\left[\frac{\Delta}{2\cos\theta}\right] \tag{6}$$

with

$$\Delta = \sqrt{\left(\frac{d}{2R}\right)^2 - 1}$$

This is a valuable result, since it is independent of the beam profile, and it is also consistent with the observed fact that the larger the Bragg angle, the less the defocusing effect. According to Fig. 2, the intensity registered by the detector should be obtained through integration on the zone II. By symmetry, zones I and III, which contain the intensity blocked by the slit, are equal to each other. When all the intensity passes the slit, assuming total reflection, the intensity

registered by the detector is the integrated intensity I_0 of the incident beam

$$I_0 = \int_0^R \int_0^{2\pi} g(r) r dr d\vartheta = 2\pi \int_0^R g(r) r dr$$

where $g(r)$ is the function which describes the profile of the primary beam, assumed to be radial. If this intensity is normalized to one, then

$$\int_0^R g(r) r dr = \frac{1}{2\pi} \tag{7}$$

According to Fig. 2, the intensity blocked by the left part of the slit is

$$I_1 = \int_{\frac{d}{2}}^{y_{\max}} \int_{x_1}^{x_2} g(x,y) dx dy$$

and the intensity I arriving at the detector is then

$$I(\chi) = 1 - 2I_1. \tag{8}$$

From Eq. (4), the limits of the integral I_1 are

$$x_{1,2} = \frac{yQ \pm \sqrt{R^2 + R^2Q^2 - y^2}}{1+Q^2}$$

where $Q = 2\cos\theta tg\chi$.

If a Lorentzian curve is used to describe the beam profile, following function is proposed

$$g(r) = A\left\{\frac{1}{B^2+r^2} - \frac{1}{B^2+R^2}\right\} \tag{9}$$

where r^2 is obtained from (4) substituting R^2 by this value, and according to (7)

$$A = \frac{1}{\pi\left\{\ln\left[1+\left(\frac{R}{B}\right)^2\right] - \left(\frac{R}{B}\right)^2 \frac{1}{1+\left(\frac{R}{B}\right)^2}\right\}}. \tag{10}$$

B is the width of the curve of the beam profile.

Numerical calculations for (8) as a function of χ were made through a computer program in Dev C++.

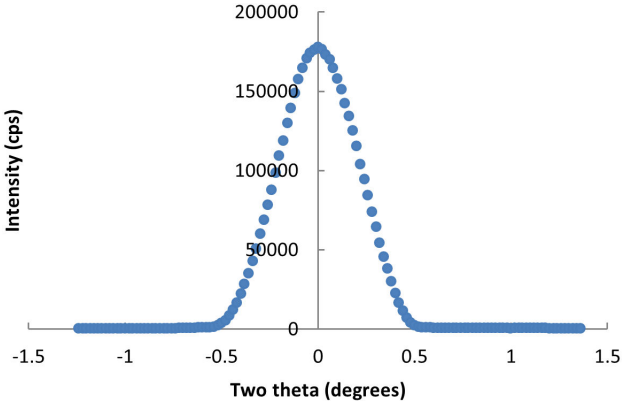

FIGURE 3. Profile of the primary beam.

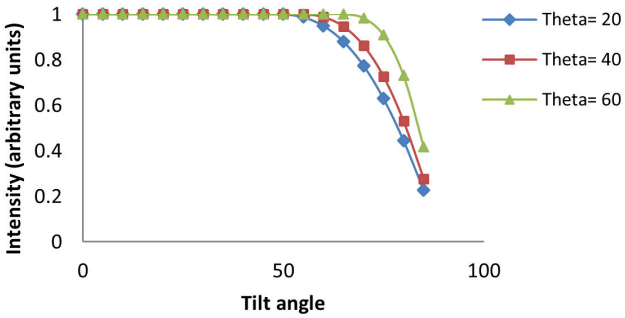

FIGURE 4. Defocusing curves obtained from the present method considering a parallel beam for three different Bragg angles. An effective beam radius of 1.3 mm was considered; the FWHM was 0.65 mm.

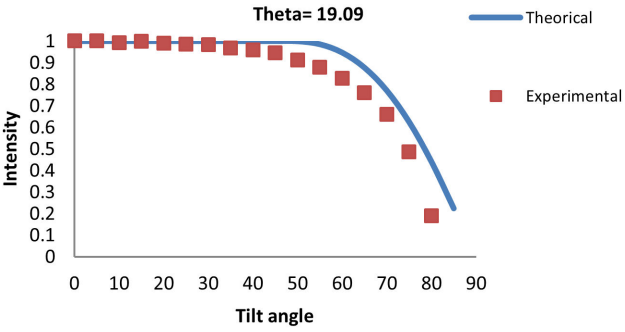

FIGURE 5. Comparison of calculated defocusing for a parallel beam, with reflection 111 of silver powder.

3. Experimental procedure

Defocusing curves of reflections 111, and 220 of copper and silver, and 222 of silver powder samples, were measured using an Eulerian goniometer associated to a D-8 Bruker X-ray diffractometer; a 1.0 mm cylindrical beam collimator was used for the incident beam, a 6 mm slit stayed in front of the detector, and the length of the detector arm was 30 cm. Copper radiation was used, and $K\beta$ component was eliminated through a Ni filter. The primary beam and zeros of theta and two theta angles were set according to the equipment conventional procedure. First, the primary beam profile was measured using a 0.05 mm slit in front of the detector. Fig. 3 shows the result. To slightly compensate the divergence of the beam, its radius at the sample place was taken as $R = 1.3$ mm for evaluations, and the width B of the beam, obtained from the FWHM of the measured curve was 0.65 mm. In order to minimize texture formation in powder during preparation, several points of the net were measured and averaged.

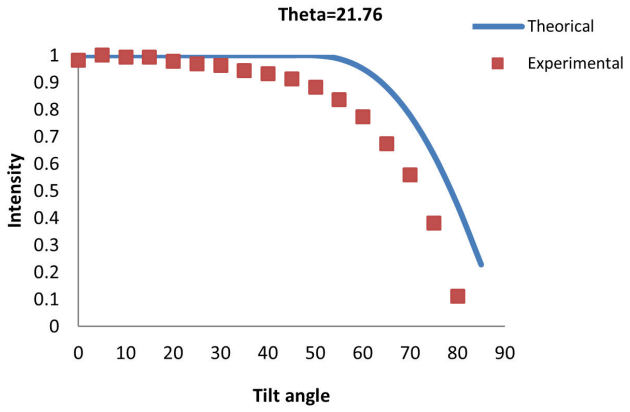

FIGURE 6. Theoretical curve and measured data for reflection 111 of copper.

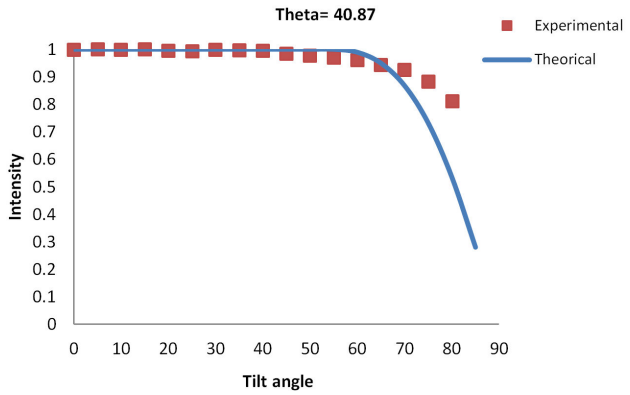

FIGURE 7. Theoretical curve and measured data for reflection 222 of silver.

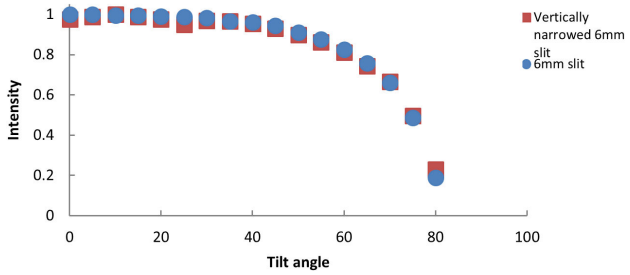

FIGURE 8. Comparison of the defocusing curve for reflection 111 of silver, measured with a narrow receiving vertical slit (squares), and with the conventional wide receiving slit (circles).

Figure 4 give defocusing results for three different Bragg angles, where it can be seen that this parallel beam approach reproduces qualitatively well the well known behavior of defocusing. Figures 5 to 7 give some results of defocusing curves for copper and silver, and the corresponding curves predicted by this method. Discrepancies of both curves should be attributed mainly to beam divergence effects on defocusing. Also, in order to appreciate the influence of the arch length of the measured Debye-Scherrer ring, a measurement was made with the receiving slit narrowed vertically to about 1 mm. Results are shown in Fig. 8, indicating no variation.

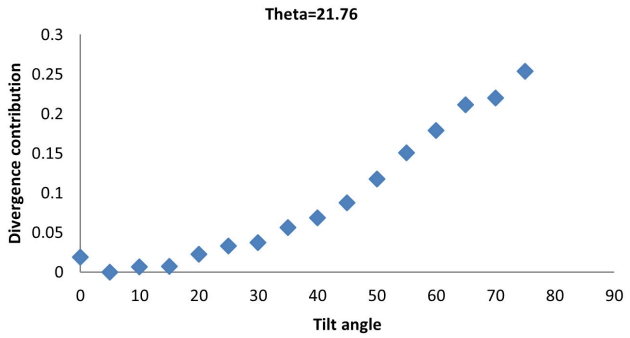

FIGURE 9. Contribution of beam divergence to defocusing for copper powder.

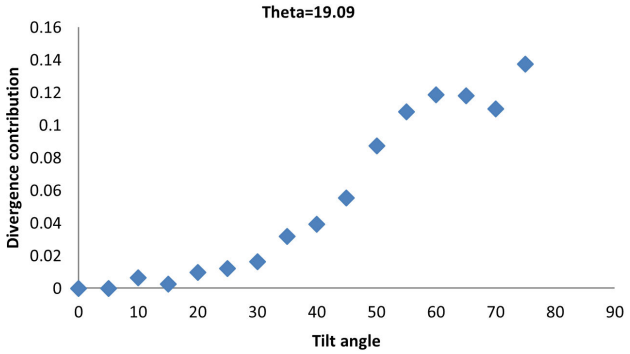

FIGURE 10. Contribution of beam divergence to defocusing for silver powder.

4. Discussion and conclusions

From Figs. 4 to 8, following can be stated: The consideration of elongation of the beam projection on the sample surface, without beam divergence, reproduces the main features of defocusing curves; the critical angle χ_0 and the dependence of the curves as a function of theta follow the well known behavior. However, χ_0 is shifted towards lower tilt angles as obtained from (6) for all defocusing curves by beam divergence. This method also predicts a sharper increase of defocusing as that observed experimentally, which can also be attributed to divergence since it tends to smear the sharpness of the beam. The difference between calculated and experimental values is mainly due to divergence, and Figs. 9 and 10 give this contribution. In general, the beam approach, as expected, predicts less defocusing than true defocusing, since divergence can only broaden the projection of the beam on the sample, and for Bragg angles up to about 40° this is actually observed. The inversion of this behavior observed for reflection 222 of silver is probably due to the Lorentzian profile of the primary beam. Actually the profile of the diffracted beam is not simple since for points along the focus line, it converges, but for other points it diverges, and the beam source is not a point. A numerical improvement of the primary beam could certainly improve results.

Additionally it has been demonstrated that a shorter height of the receiving slit reduces intensity, but does not affect defocusing.

Acknowledgments

One of us (J. Palacios) wants to acknowledge his institution for granting the project as sabbatical leave.

1. L.G. Schulz, *J. Appl. Phys*. **20** (1949) 1030.
2. B. Gale and D. Griffiths, *Brit. J. Appl. Phys.* **11** (1960) 96.
3. E. Tenckhoff, *J. Appl. Phys.* **41** (1970) 3944.
4. J.C. Couterne and G. Cizeron, *J. Appl. Cryst.* **4** (1971) 461.
5. A. Segmüller, *J. Appl. Phys.* **43** (1972) 2907.
6. C.K. Chow, *Met. Trans. A* **16A** (1985) 299.
7. U. Welzel and M. Leoni, *J. Appl. Cryst.* **35** (2002) 196.
8. D. Chateigner, *Combined Analysis: Structure-texture microstructure-phase-stresses-reflectivity determination by X-ray and neutron scattering*, (Wiley-ISTE, 2010).
9. Y. Perlovich, H.J. Bunge and M. Isaenkova, *Textures & Microstructures*, **29** (1997) 241-266.
10. F. Cruz-Gandarilla, A.M. Salcedo-Garrido, T. Baudin, H. Mendoza-León, R. Penelle, *Materials Science Forum Vols*. **702-703** (2012) 519.
11. J. Palacios Gómez, T. Kryshtab and C.A. Vega Rasgado, Z. Kristallogr, *Proc.* **1** (2011) 119.
12. A. Cadena Arenas, T. Kryshtab, J. Palacios Gómez, and A. Kryvko, *Ingeniería, Investigación y Tecnología*, **XV** (2014) 241.